Article

Coverage enhancement accelerates acidic CO_2 electrolysis at ampere-level current with high energy and carbon efficiencies

Xiaohan Yu[1,3], Yuting Xu[2,3], Le Li[1,3], Mingzhe Zhang[1], Wenhao Qin[1], Fanglin Che [2,4] ✉ & Miao Zhong [1,4] ✉

Acidic CO_2 electroreduction (CO_2R) using renewable electricity holds promise for high-efficiency generation of storable liquid chemicals with up to 100% CO_2 utilization. However, the strong parasitic hydrogen evolution reaction (HER) limits its selectivity and energy efficiency (EE), especially at ampere-level current densities. Here we present that enhancing CO_2R intermediate coverage on catalysts promotes CO_2R and concurrently suppresses HER. We identified and engineered robust Cu_6Sn_5 catalysts with strong $^*OCHO$ affinity and weak $^*H$ binding, achieving 91% Faradaic efficiency (FE) for formic acid (FA) production at $1.2\,A\,cm^{-2}$ and pH 1. Notably, the single-pass carbon efficiency reaches a new benchmark of 77.4% at $0.5\,A\,cm^{-2}$ over 300 hours. In situ electrochemical Fourier-transform infrared spectroscopy revealed Cu_6Sn_5 enhances $^*OCHO$ coverage ~2.8× compared to Sn at pH 1. Using a cation-free, solid-state-electrolyte-based membrane-electrode-assembly, we produce 0.36 M pure FA at 88% FE over 130 hours with a marked full-cell EE of 37%.

The electrochemical reduction of CO_2 (CO_2R) to valuable short-chain liquid feedstocks presents an elegant solution for storing intermittent renewable electricity, while also mitigating excessive CO_2 emissions resulting from the consumption of fossil fuels[1–3]. In recent decades, significant progress has been made in understanding CO_2R reaction pathways on catalysts and the associated energetics to control CO_2R selectivity, and in developing gas-diffusion-electrode-based membrane-electrode-assembly (MEA) electrolyzers capable of achieving industrially relevant CO_2R current densities over hundreds of $mA\,cm^{-2}$ [4–7]. Despite these efforts, further advancements in CO_2R technology will depend on improving full-cell energy efficiency (i.e., power-to-product efficiency) and maximizing CO_2 utilization efficiency (i.e., CO_2-to-product conversion).

Operating CO_2R in acidic electrolytes offers a potential approach to address significant CO_2 losses caused by the reaction between CO_2 and OH^- in electrolytes to form CO_3^{2-} during CO_2R in alkaline or neutral media. In strong acids with an electrolyte pH ≤ 1, carbonate formation

is rare[8]. However, the kinetics of CO_2R under such highly acidic conditions become retarded. Additionally, the substantial increase in surface $^*H$ coverage on catalyst surfaces causes a strong competing hydrogen evolution reaction (HER), resulting in a largely reduced Faradaic efficiency (FE) for CO_2R[9,10].

Early studies have shown that increasing the local concentrations of alkali metal cations in close proximity to catalyst surfaces can enhance CO_2R by stabilizing the surface-adsorbed CO_2 and CO_2R-related intermediates through non-covalent interactions, and, at the same time, impeding the diffusion of protons to the catalyst surfaces[11–13]. However, when the system operates at high potentials (i.e. high current densities), the electroconvective flows near the electrodes become turbulent and disordered. According to the Nernst-Planck equation, this turbulence can cause a fluctuation in cation concentrations near the electrode surface, leading to variations in the local electrical field that may have the potential to disrupt the beneficial cation effect on CO_2R[14]. Prior studies have shown that

[1]College of Engineering and Applied Sciences, Collaborative Innovation Center of Advanced Microstructures, National Laboratory of Solid State Microstructures, the Frontiers Science Center for Critical Earth Material Cycling, Nanjing University, Nanjing 210093, China. [2]Department of Chemical Engineering, University of Massachusetts Lowell, Lowell, MA 01854, USA. [3]These authors contributed equally: Xiaohan Yu, Yuting Xu, Le Li. [4]These authors jointly supervised this work: Fanglin Che, Miao Zhong. ✉e-mail: Fanglin_Che@uml.edu; miaozhong@nju.edu.cn

applying a micrometer-thick layer of nanoparticles as a surface coating layer on catalysts mitigates the irregularities in electro-convective flows within the coated microstructures, which helps maintain a steady concentration profile of alkali metal cations[15–17]. Despite this advancement in mitigating HER, the high local concentration of alkali metal cations can lead to bicarbonate precipitation in the gas diffusion electrodes. The accumulation of bicarbonates hinders CO_2 diffusion and hampers CO_2R efficiency. To address the bicarbonate precipitation challenge, strategies involve modifying catalysts with immobilized cation groups[18] or exploring CO_2R in cation-free systems such as using solid-state-electrolyte (SSE) based MEA electrolyzers[19]. One priority for implementing these approaches is to develop efficient catalysts that can inherently promote CO_2R over the competing HER, particularly under strongly acidic conditions.

In this study, we employed computational investigations to discover a Cu_6Sn_5 catalyst with a notable abundance of surface adsorption sites having a large binding energy difference between ˙OCHO (the intermediate for formic acid (FA) production) and ˙COOH (the intermediate for CO production) while also having weaker binding to ˙H. This configuration allows for maximum selectivity in favor of producing FA over CO and other hydrocarbons while simultaneously suppressing HER.

We experimentally constructed Cu_6Sn_5 alloy catalysts on polytetrafluoroethylene (PTFE) gas diffusion electrodes using thermal vapor deposition. In situ electrochemical attenuated total reflection Fourier-transform infrared (ATR-FTIR) spectroscopy analysis revealed a notable enhancement showcasing a ~2.8 elevation in ˙OCHO coverage on Cu_6Sn_5 compared to control catalysts of Sn, operating under identical electrochemical conditions at pH = 1. The active Cu_6Sn_5 achieves a high FE of 91% for FA production at a current density of 1.2 A cm⁻² in a strongly acidic electrolyte at pH = 1. Furthermore, it shows a marked single-pass carbon efficiency (SPCE) of 77.4% at 0.5 A cm⁻², representing approximately 2.8-fold enhancement in the SPCE compared to the prior report of ~27.4% obtained at ~0.24 A cm⁻² [20]. Such notable performance was stable over 300 h of

continuous acidic CO_2R at 0.5 A cm⁻² in a flow-cell electrolyzer at pH = 1.

When integrating Cu_6Sn_5 into a cation-free, SSE-based MEA electrolyzer, we produced 2.6 liters of 0.36 M pure FA at 100 mA cm⁻² (area: 4 cm²) over 130 h at a production rate of 5 mL cm⁻² h⁻¹, along with a full-cell energy efficiency of 37%. These results feature the potential of enhancing surface intermediate coverage as an efficient means for acidic CO_2R, particularly in cation-free systems at industrially relevant current densities.

Results

Density functional theory (DFT) studies

Copper (Cu) has established itself as a predominant and cost-effective electrocatalyst capable of generating a variety of hydrocarbons through CO_2R. Previous research has revealed effective strategies for modifying the ˙CO-binding and ˙OCHO-binding properties on surfaces of Cu-based alloy surfaces by introducing foreign elements (e.g., Zn, Al, Pb) into the Cu lattice. Specifically, the inclusion of 5–10 at.% Zn or Al into Cu has shown the ability to partially weaken ˙CO adsorption on the Al or Zn modified Cu site compared to the adjacent Cu-Cu site, thereby creating asymmetric ˙CO binding energies for improved C_{2+} production[16,17]. Additionally, the introduction of a single Pb atom into Cu has been observed to enhance selectivity towards formic acid[21]. These alternations selectively promote the production of CO/C_{2+} or FA via distinctive reaction pathways (Fig. 1a). To further curb the competing HER in strong acids, two major approaches are considered: (1) employing alkali metal cations to hamper H⁺ diffusion toward catalyst surfaces, and (2) augmenting the coverage of surface CO_2R intermediates to outcompete the HER.

As a representative p-block metal, Sn has a relatively stronger oxygen affinity and weaker adsorption energy for ˙H than pristine Cu. It can also form alloys with Cu across the entire concentration profile ranging from 0% to 100%. Interestingly, a previous study has investigated the relationship between CO_2R-to-FA activity and the ˙OCHO adsorption energy with various metal catalysts[22], and identified Sn and Cu as promising candidates for selective FA production due to their
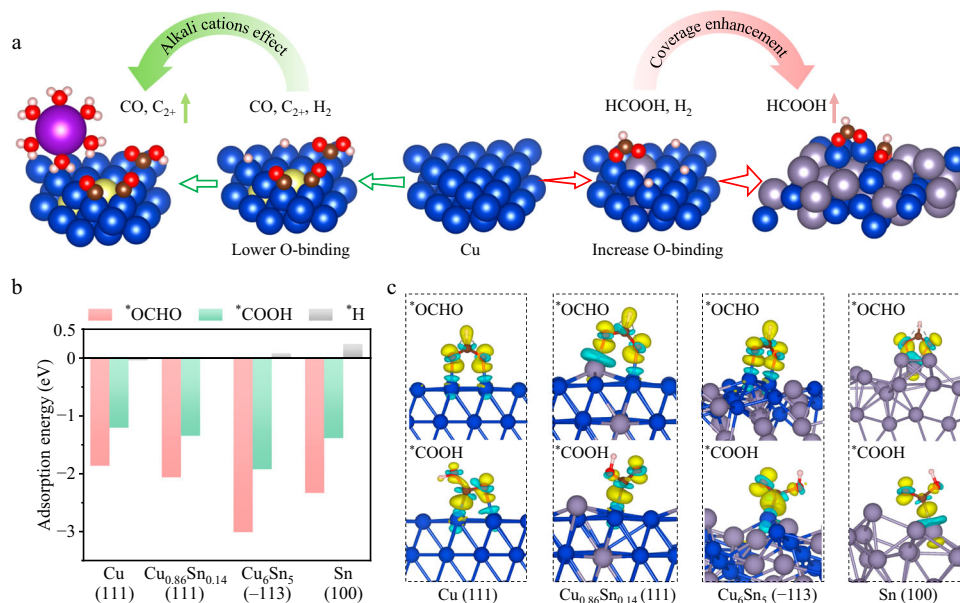

Fig. 1 | DFT calculations. a Schematic representation of CO_2R and HER on Cu-based catalysts incorporated with different metal atoms, along with alkali cations effect and coverage enhancement strategy. Color-coded atoms represent Cu (blue), Sn (grey), Zn or Al (yellow), K (purple), O (red), C (brown), and H (pink). **b** The calculated adsorption energy of ˙OCHO, ˙COOH, and ˙H on Cu, $Cu_{1-x}Sn_x$ (x = 0.14, 0.44), and Sn catalysts. Since the ˙H adsorption energies (referring to 1/2

H_2) over Cu and $Cu_{0.86}Sn_{0.14}$ are −0.03 eV and −0.02 eV, it is hard to distinguish their values in the plot. **c** Differential charge density plots illustrating the enhanced charge transfer between the Cu_6Sn_5 (−113) surface and ˙OCHO compared to the other examined surfaces. The isosurface level of the differential charge densities is 0.0045 e/bohr³. The yellow or blue areas represent a gain or loss of electrons.
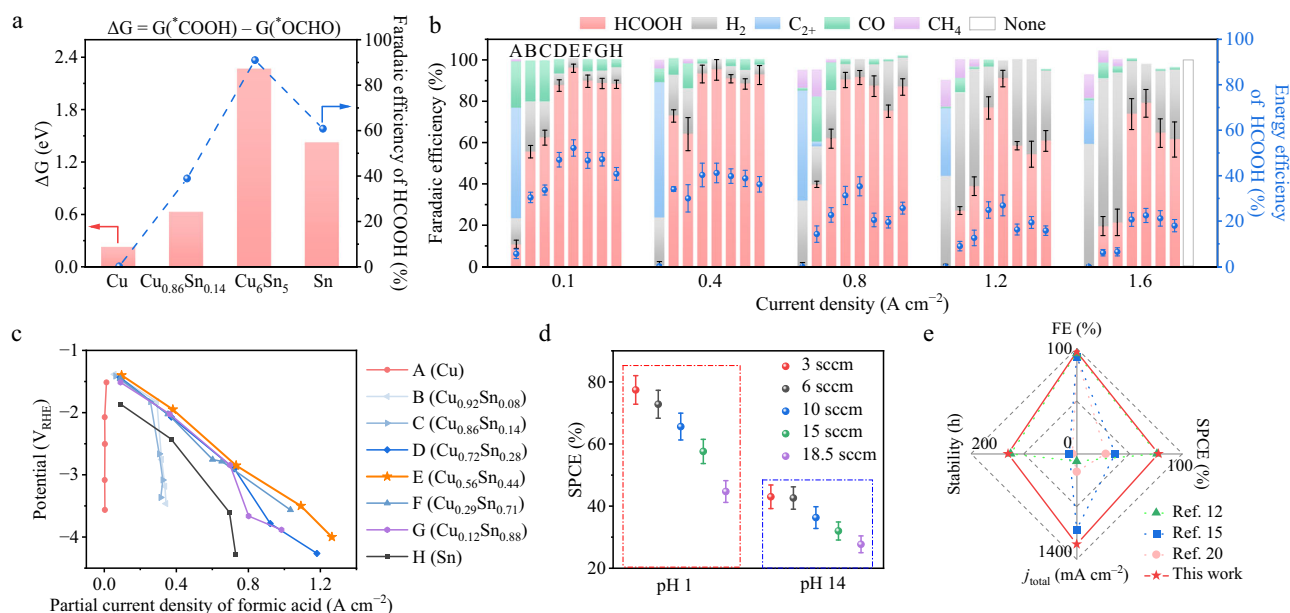
Fig. 2 | Electrochemical performance of CO₂ reduction with Cu, Cu₁₋ₓSnₓ (x = 0.08, 0.14, 0.28, 0.44, 0.71, 0.88) and Sn catalysts in 3 M KCl and 0.05 M H₂SO₄ electrolyte at pH 1 in flow cells. a A volcano-like plot showing the Gibbs free energy difference (ΔG) between *OCHO (an intermediate for FA production) and *COOH (an intermediate for CO production) over Cu (111), Cu₀.₈₆Sn₀.₁₄ (111), Cu₆Sn₅ (−113), and Sn (100) surfaces. This plot is in line with the obtained experimental data of Faradaic efficiency (FE) for FA production at 1.2 A cm⁻² in 3 M KCl and 0.05 M H₂SO₄. Gibbs free energy was calculated at room temperature (298.15 K), pH of 1, and an applied potential of −2.1 V vs. reversible hydrogen electrode (V_RHE) using computational hydrogen electrode (CHE) model. **b** Distributions of Faradaic

efficiencies (FE) for formic acid (FA), H₂, C₂₊, CO, and CH₄ at 0.1, 0.4, 0.8, 1.2, and 1.6 A cm⁻². The error bars presented are derived from three independent tests. **c** Partial current densities of FA as a function of the applied potentials on Cu, Cu₁₋ₓSnₓ (x = 0.08, 0.14, 0.28, 0.44, 0.71, 0.88), and Sn catalysts. **d** Single-pass carbon efficiency (SPCE) of CO₂R on Cu₆Sn₅ at 0.5 A cm⁻², obtained at pH 1 and 14 at different CO₂ flow rates of 3, 6, 10, 15, 18.5 standard cubic centimeter per minute (sccm). The error bars presented are derived from three independent tests. **e** Performance comparison of this study and the previously published data under acidic conditions.

favorable *OCHO adsorption energies. With this insight, we aimed to create Cu-Sn alloys that could further fine-tune the *OCHO adsorption close to the optimal adsorption-energy values in the adsorption-activity trend. This would contribute to the improvement of the selectivity and activity in the CO₂R-to-FA conversion.

To understand the role of Sn in the Cu₁₋ₓSnₓ (x = 0.14, 0.44) catalysts in tuning the catalytic selectivity of CO₂R to CO and FA, we built surfaces with various Cu/Sn ratios from pure Cu to Cu₁₋ₓSnₓ alloy, and then to pure Sn, and used DFT to calculate the Gibbs free energetic diagrams for CO and FA generation. Based on the previous literature reviews[23,24], the potential rate-determining step (RDS) for the CO₂R-to-CO conversion is the first proton transfer to form *COOH from CO₂ (CO₂ (gas) + H⁺ + e⁻ + * → *COOH), while the potential RDS for CO₂R-to-FA is the first proton transfer to form *OCHO (CO₂ (gas) + H⁺ + e⁻ + * → *OCHO). By using DFT calculations, we identified that the Cu₆Sn₅ alloy possesses a high abundance of surface sites with a stronger binding affinity to *OCHO compared to *COOH, making it thermodynamically more favorable for producing FA (Fig. 1b). In addition, Cu₆Sn₅ exhibits notably weaker binding to *H (+ 0.33 eV referring to 1/2 H₂), resulting in a substantial energy requirement for H₂ production and thus, suppressing HER.

To study how the electronic properties of the surface-active sites on Cu₁₋ₓSnₓ catalysts with varying Sn concentrations affect the selectivity of FA and CO production, we calculated the differential charge density of *OCHO and *COOH over the experimentally observed surfaces in Fig. 1c. Our results indicate that the Cu₆Sn₅ (−113) surface exhibits more charge transfer with *OCHO than that over other examined surfaces. This charge analysis is consistent with the adsorption energy calculation, where the Cu₆Sn₅ (−113) surface exhibits the strongest adsorption energy of *OCHO among all the examined surfaces. Such strong adsorption energy of *OCHO also indicates a potentially high surface coverage of *OCHO over the

Cu₆Sn₅ (−113) surface. In addition, since two O−Cu bonds are formed between O^δ⁻ of *OCHO and Cu atoms on Cu₁₋ₓSnₓ surfaces, our results show that Cu₆Sn₅ (−113) surface presents -1.3 and -2.3 eV more favorable formation energy for *OCHO than for *COOH under alkaline (Supplementary Fig. 1) and acidic (Fig. 2a) conditions, respectively. Furthermore, according to the experimental results in Fig. 2b, the production of C₂₊ and CH₄ products disappeared over the metal surface when the concentration of Sn in Cu₁₋ₓSnₓ catalysts was increased to -14%. To reveal the role of Sn in Cu₁₋ₓSnₓ catalysts in eliminating the C₂₊ and CH₄ production during CO₂R, we compared the adsorption energy of CO over pure Cu (111) and Cu₀.₈₆Sn₀.₁₄ (111) surfaces (Supplementary Fig. 2). The DFT results show that the presence of Sn on the Cu₀.₈₆Sn₀.₁₄ (111) surface weakens the adsorption of CO to -0 eV compared to −0.08 eV on the pure Cu (111) surface. Thus, CO will likely desorb from the Cu₀.₈₆Sn₀.₁₄ (111) surface and be unable to hydrogenate via H protonation to produce CH₄ or couple with another adsorbed *CO intermediate to generate C₂₊ species. These findings are in agreement with previous literature reports and experiments that have observed no C₂₊ and CH₄ species produced over Cu₀.₈₆Sn₀.₁₄[25,26].

We performed Gibbs free energy calculations to quantitatively determine the reaction energy difference between the reaction pathways of CO₂-*COOH−CO/C₂₊ and CO₂-*OCHO−HCOO⁻ over the experimentally observed surfaces, including Cu (111), Cu₀.₈₆Sn₀.₁₄ (111), Cu₆Sn₅ (−113), and Sn (100) surfaces, where the possible reaction mechanisms have been shown in Supplementary Fig. 3. These calculated surfaces are the dominant facets in XRD measurement in Supplementary Figs. 4−9 and Supplementary Table 1. Gibbs free energetic diagrams for the formation of *OCHO and *COOH over different catalytic surfaces were constructed according to the experimental conditions of room temperature, pH 1 of the electrolyte, and an applied potential of −2.1 V vs. RHE (V_RHE). Our theoretical results (Fig. 2a,

Supplementary Figs. 10–33) show that the Gibbs free energy differences ($\Delta G = G(^*COOH) - G(^*OCHO)$) of the potential RDSs of FA and CO pathways during CO_2R present a volcano-like plot as increasing the concentration of Sn in the $Cu_{1-x}Sn_x$ catalysts. Among the four examined surfaces, Cu_6Sn_5 (−113) shows the largest ΔG between the CO_2R to FA and CO pathways, indicating that Cu_6Sn_5 (−113) contributes the highest selectivity for FA production. The theoretical results are consistent with the experimental results (Fig. 2b, c) that the FE of FA production over Cu_6Sn_5 is the highest.

To examine the competitive HER over Cu (111), $Cu_{0.86}Sn_{0.14}$ (111), Cu_6Sn_5 (−113) and Sn (100) surfaces, we examined the energy diagram of HER (Supplementary Fig. 34). The corresponding $^*H$ adsorption configurations can be seen in Supplementary Figs. 35–38. The increased free energy of HER indicates that the HER will be suppressed, and the selectivity for CO_2R can thus be improved over $Cu_{0.86}Sn_{0.14}$, Cu_6Sn_5, and Sn compared to that on pristine Cu. This is consistent with experimental results (Fig. 2b), which show the FE of HER over Cu is higher than that on $Cu_{0.86}Sn_{0.14}$, Cu_6Sn_5, and Sn.

Finally, we built surfaces with different Cu/Sn ratios, ranging from pure Cu to $Cu_{1-x}Sn_x$ alloy, and then to pure Sn. Using DFT calculations, we analyzed the surface formation energetics for each surface. As depicted in Supplementary Fig. 39, Cu_6Sn_5 (−113) shows improved stability with a lower surface formation energy compared to the pristine Cu (111) facet. Conversely, Sn (100) shows poor stability with a higher surface formation energy.

Electrochemical CO_2R studies

With the theoretical insight, we conducted a systematical investigation into the Cu−Sn alloy as an illustrative catalyst system with the objective of obtaining exclusive CO_2R to HCOOH at high current densities while also achieving high energy and carbon efficiencies. Experimentally, we created $Cu_{1-x}Sn_x$ ($x = 0.08, 0.14, 0.28, 0.44, 0.71, 0.88$) and control catalysts of pure Cu and Sn on PTFE gas diffusion electrodes using thermal evaporation (Supplementary Figs. 4 and 40, 41). We evaluated their CO_2R performance for $Cu_{1-x}Sn_x$ ($x = 0.08, 0.14, 0.28, 0.44, 0.71, 0.88$) and controlled Cu and Sn catalysts in a flow cell with a three-electrode configuration in both alkaline and acid electrolytes. We quantitatively analyzed the gas and liquid products using gas chromatography (GC), nuclear magnetic resonance spectroscopy (NMR), and ion chromatography (IC).

In a 1 M KOH electrolyte at pH 14, the linear sweep voltammetry (LSV) curves in Supplementary Fig. 42 showed a sharp increase in the current densities with the increase of applied negative potentials, indicating efficient electrical conductivity for the Cu and $Cu_{1-x}Sn_x$ ($x < 0.71$) electrodes. With the addition of Cu in $Cu_{1-x}Sn_x$ ($x < 0.71$), the onset potential for formate shifted positively, indicating improved CO_2R kinetics. At high current densities, Cu_6Sn_5 also displayed the highest selectivity for formate production, with over 90% formate FEs across a wide current density range of 0.4 to 1.2 A cm^{-2} (Supplementary Fig. 43). The Cu_6Sn_5 catalyst showed formate partial current densities of up to -1.5 A cm^{-2} at a relatively low operating potential of around −1.8 V_{RHE} (Supplementary Fig. 44) and the highest formate selectivity close to 90% (Supplementary Fig. 43).

To assess the stability of Cu_6Sn_5 in 1 M KOH, we carried out Galvanostatic tests using an alternating current density mode (0.05 A cm^{-2} for 30 s and 0.5 A cm^{-2} for 90 s)[17] for 160 hours in a flow cell (Supplementary Fig. 45). Prior to the stability test, we coated a carbon-Nafion™ or SiC-Nafion™ mixed layer with a thickness of 2–5 μm on the surface of Cu_6Sn_5 to enable a uniform electrohydrodynamic flow near the catalysts[14]. Through the 120-h CO_2R operation at a current density of 0.5 A cm^{-2}, we obtained a stable formate FE of above 85%. When comparing the FE and current density of this work with the previous reports under alkaline conditions, we found that we found that our results are superior (Supplementary Fig. 46 and Supplementary Table 2)[6,11,19,21,27–44].

In 3 M KCl and 0.05 M H_2SO_4 electrolyte at pH 1, Cu_6Sn_5 exhibited the highest selectivity, reaching up to 96% at −1.4 V_{RHE} for formic acid in Fig. 2c. Remarkably, Cu_6Sn_5 showed a high FE of above 90% for FA production across a wide range of current densities from 0.4 to 1.2 A cm^{-2} (Fig. 2b). We examined the SPCE for Cu_6Sn_5 under a constant current density of 0.5 A cm^{-2} in a flow cell equipped with a 1.7 × 1.7 cm^2 serpentine channel reaction area at various CO_2 flow rates and electrolyte pH levels (more details are presented in the Supplementary Information)[15]. Figure 2d presents a maximum SPCE of 77.4%, achieved at a CO_2 flow rate of 3 standard cubic centimeter per minute (sccm) under pH 1 conditions. The electrode of Cu_6Sn_5 coated with carbon-Nafion™ or SiC-Nafion™ demonstrated stable FA production for over 300 hours, maintaining over 70% FE at a cathodic potential of −2.5 V_{RHE}. This equated to a 40% cathodic energy efficiency (CEE) at 0.5 A cm^{-2} at pH 1 (Supplementary Fig. 47). Theoretical investigations were correspondingly carried out in this segment to investigate the effects of the electrochemical operating environment effects (e.g., electrolyte of 3 M K$^+$, applied potential of −2.1 V_{RHE}, and pH = 1) on the selectivity for FA vs. CO formation using Constant Electrode Potential (CEP) model via performing Grand canonical DFT calculations[45–49]. The selectivity for FA across Cu (111), $Cu_{0.86}Sn_{0.14}$ (111), Cu_6Sn_5 (−113), and Sn (100) surfaces exhibits a volcano plot (Fig. 2a and Supplementary Fig. 48), with Cu_6Sn_5 (−113) displaying the highest energy difference between the two pivotal intermediates, favoring the adsorption of $^*OCHO$ over CO. More details regarding grand canonical DFT simulations are provided in Supplementary Information. We compared this work with previously reported results on the CO_2R-to-FA production under acidic conditions in terms of elevated current density, FE, SPCE, and stability in Fig. 2e[12,15,20].

Characterization

We conducted material and structure characterizations, as well as surface wettability analysis, for the Cu_6Sn_5 catalyst before the CO_2R reaction. Figure 3a shows a schematic of the CO_2R process on Cu_6Sn_5/PTFE electrodes. The cross-sectional scanning electron microscope (SEM) image in Fig. 3b shows the well-defined structure of Cu_6Sn_5 nano-to-micro particles densely packed on the PTFE substrate. This Cu_6Sn_5-on-PTFE structure was synthesized over a large scale via thermal evaporation (Fig. 3c and Supplementary Fig. 49), exhibiting hydrophobicity, as indicated by a water contact angle of 128° (Fig. 3c). This hydrophobicity enables CO_2 diffusion through the gaps between the particles on the PTFE sides to the catalyst surface (Fig. 3a). The top-view SEM presents that the diameter of the Cu_6Sn_5 particles is 300–600 nm (Fig. 3d). Energy dispersive X-ray spectroscopy in transmission electron microscopy (STEM-EDX) analysis revealed a uniform distribution of Sn and Cu over the majority of the Cu_6Sn_5 particles (Fig. 3e).

Detailed structural analysis using transmission electron microscope (TEM), high-resolution transmission electron microscope (HRTEM), and selective area electron diffraction (SAED) analyses (Fig. 3f, g) confirmed the formation of monoclinic Cu_6Sn_5 crystal. These results are in line with the X-ray powder diffraction (XRD) patterns in Supplementary Fig. 50, which indicate the presence of the main (−113), (132), and (−314) facets for Cu_6Sn_5. More details regarding the crystallographic and material analysis of catalysts after acidic CO_2R operation are presented in Supplementary Figs. 51–53.

In situ ATR-FTIR analysis

We used in situ ATR-FTIR spectroscopy to study CO_2R intermediates coverage on Cu_6Sn_5-on-PTFE, Cu-on-PTFE, and Sn-on-PTFE electrodes during acidic CO_2R electrolysis in the same pH 1 electrolyte of 3 M KCl and 0.05 M H_2SO_4, spanning a range of applied potentials from −0.24 to −1.64 V_{RHE}. We also incorporated an internal standard of potassium ferricyanide in the electrolytes to facilitate peak area calibration. In the
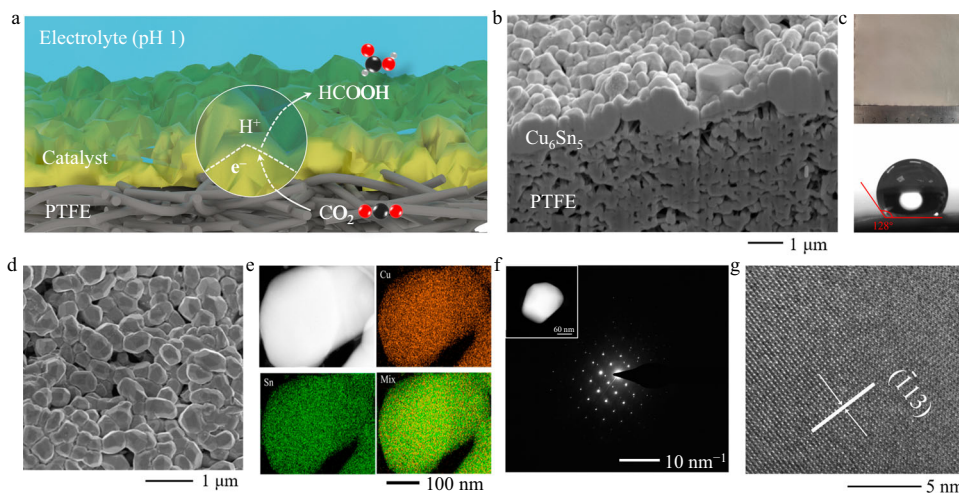
Fig. 3 | Characterizations of the thermally evaporated Cu$_6$Sn$_5$-on-PTFE electrodes. a Schematic representation of the CO$_2$R process on Cu$_6$Sn$_5$-on-PTFE electrodes. **b** Cross-sectional SEM image of the Cu$_6$Sn$_5$/PTFE electrode, showcasing the dense arrangement of Cu$_6$Sn$_5$ nano-to-micro particles on the PTFE substrate. **c** Optical image and the measured contact angle of a water droplet on the Cu$_6$Sn$_5$-on-PTFE electrode. **d–g** Top-view SEM image (**d**), STEM-EDX images (**e**), HAADF image and SAED pattern (**f**), and HRTEM image (**g**) of the thermally evaporated Cu$_6$Sn$_5$ catalyst.
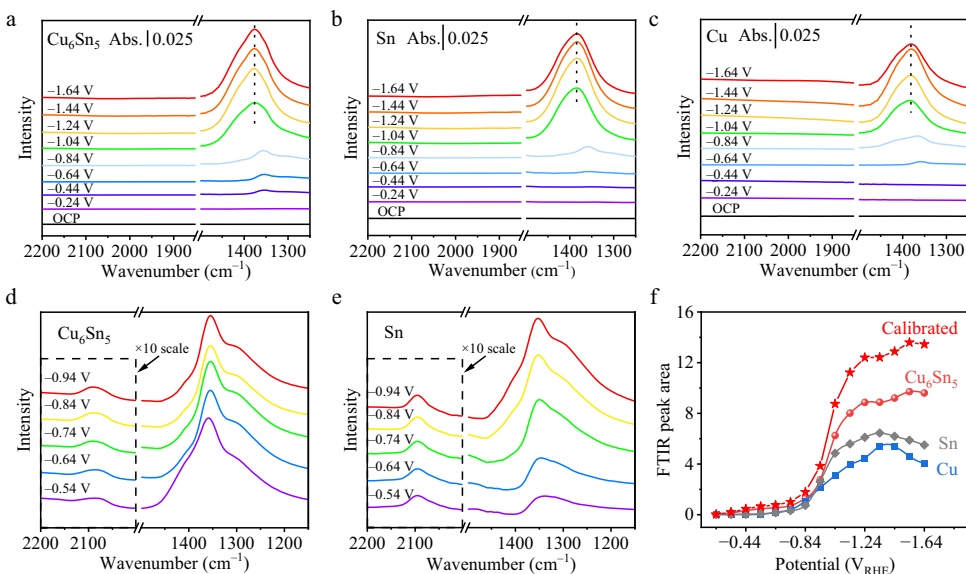

Fig. 4 | In situ ATR-FTIR spectroscopy analysis. a–c In situ ATR-FTIR spectra measured at different applied potentials for Cu$_6$Sn$_5$ (**a**), Sn (**b**), and Cu (**c**) under identical electrochemical conditions at pH = 1. Abs. stands for absorbance. **d, e** ATR-FTIR results of Cu$_6$Sn$_5$ (**d**), and Sn (**e**) in the potential range of −0.54 to −0.94 V$_{RHE}$, which were used to calculate the relative peak areas of *OCHO using the peak areas of the potassium ferricyanide as a reference. The peak intensities of the internal standard potassium ferricyanide in panels (**d**) and (**e**) have been magnified by 10 times to facilitate comparison with those of the *OCHO intermediates. **f** The integrated ATR-FTIR peak areas of the Cu, Sn, Cu$_6$Sn$_5$ with and without calibration.

ATR-FTIR spectra for the Cu$_6$Sn$_5$ and Sn catalysts (Fig. 4a–c), significant peaks were absent within the range of 1900 to 2200 cm^{-1}. In contrast, distinct infrared vibration bands related to the *OCHO intermediate were observed within the 1375–1385 cm^{-1} range for all Cu$_6$Sn$_5$, Cu, and Sn catalysts. The onset potential for the *OCHO intermediate on Cu$_6$Sn$_5$ was −0.44 V$_{RHE}$, lower than that on Cu and Sn, indicating fast CO$_2$R-to-HCOOH kinetics with Cu$_6$Sn$_5$. During the in situ ATR-FTIR test using a 5 mM potassium ferricyanide internal standard in 3 M KCl and 0.05 M H$_2$SO$_4$, we observed a constant peak area for potassium ferricyanide within the potential range of −0.54 to −0.94 V$_{RHE}$. Consequently, we established a calibration curve within this potential range, using the potassium ferricyanide peak as a reference. This allowed us to calculate the peak areas of *OCHO intermediates on different catalysts at the same potential range (Fig. 4d, e and Supplementary Table 3). Notably, adhering the established calibration relationship, the plateau *OCHO peak intensity on Cu$_6$Sn$_5$ measured at potentials above −1.04 V$_{RHE}$ in the CO$_2$R electrolyte is ~2.8 times higher than that of Sn, with all measurements conducted under identical conditions (Fig. 4f). These results point toward an enhanced surface coverage of *OCHO on Cu$_6$Sn$_5$, which facilitates selective FA production during acidic CO$_2$R.

To produce a pure formic acid solution, we conducted CO$_2$R using an AEM (Sustainion X37-50 Grade) based SSE-MEA electrolyzer. 0.5 M H$_2$SO$_4$ was used as the anolyte and IrO$_x$/Ti foam was used as the anode (Fig. 5a). During the electrolysis, HCOO$^-$ was generated on the cathode side and diffused through the AEM into the middle SSE layer.
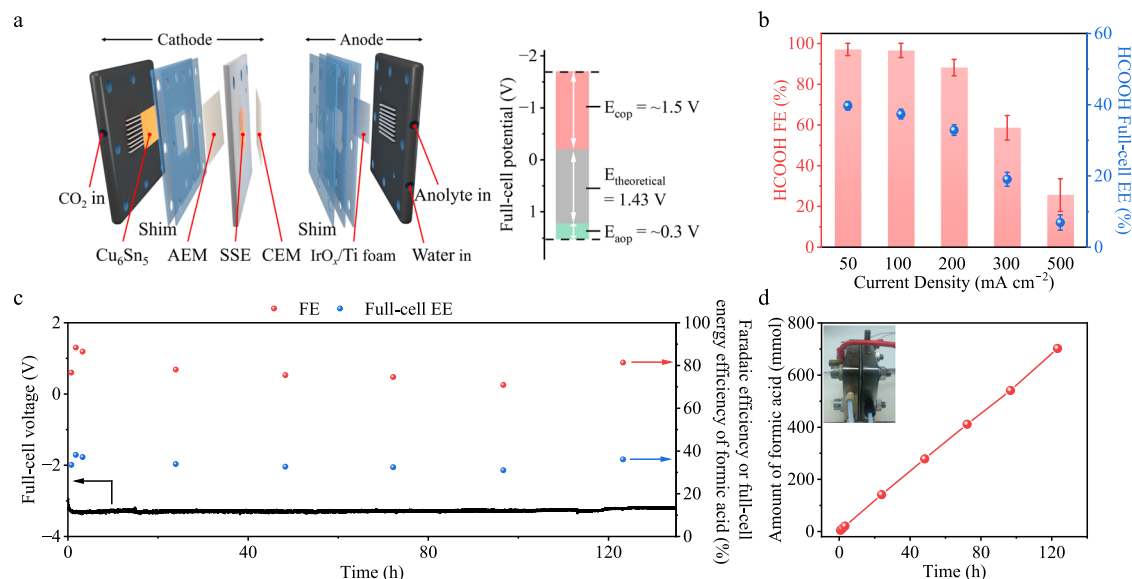
Fig. 5 | Electrochemical CO₂R performance with Cu₆Sn₅ in acidic electrolytes at pH 1. a Structure of a solid-state-electrolyte-based membrane electrode assembly electrolyzer for CO₂R and its potential distribution. **b** FEs and full-cell energy efficiencies of FA production with Cu₆Sn₅ at different current densities. The error bars presented are derived from three independent tests. **c** FEs and full-cell energy efficiencies of FA production with Cu₆Sn₅ at 100 mA cm⁻² during 130-h CO₂R operation. **d** Optical image of MEA and production rate of FA with Cu₆Sn₅ at 100 mA cm⁻² during 130-h CO₂R operation.

Simultaneously, H^+ permeated through the CEM (Nafion 117) and reacted with $HCOO^-$ to form FA. The produced FA solution was collected by passing deionized water through the SSE layer. As shown in Fig. 5a, the operating potential is 3.4 V for the overall CO_2-to-FA and H_2O-to-O_2 reaction in an SSE-based MEA electrolyzer. The detailed potential distributions are listed in Fig. 5a: a theoretical potential of 1.43 V required to initiate the CO_2R-to-FA reaction, a -0.3 V overpotential on the IrO_x loaded Ti mesh anode, and an -1.5 V overpotential on the SSE, anion and cation membranes, and Cu_6Sn_5 cathode. In Fig. 5b, using the Cu_6Sn_5 catalyst, the FA FE reached ~96% at 100 mA cm⁻². The full-cell voltage was −3.7 V and the full-cell energy efficiency was over 37%. We evaluated the CO_2R performance in different anolytes (0.1 M, 0.5 M, and 1 M H_2SO_4) in Supplementary Fig. 54. We quantified the amount of FA produced using IC, NMR, and pH measurements (Supplementary Fig. 55). The results confirmed the production of 2.6 liters of 0.36 M pure FA solution (Supplementary Fig. 56) with a production rate of 5 mL cm⁻² h⁻¹ (20 mL h⁻¹) over a continuous 130-h CO_2R process (Fig. 5c). Figure 5d shows an optical image of an SSE-based MEA and a steady production rate of FA over the 130-h CO_2R process to produce ~700 mmol pure FA.

Discussion

In this study, we demonstrate the effectiveness of enhancing surface coverage of CO_2R intermediates as a strategy to promote CO_2R at ampere-level current densities and under strongly acidic conditions. Theoretical DFT calculations have revealed that Cu_6Sn_5 enhances the adsorption of *OCHO compared to *COOH and *H, resulting in increased surface *OCHO coverage and promoted FA production in CO_2R while simultaneously suppressing the HER. Experiments have identified a robust Cu_6Sn_5 catalyst that exhibits exclusive FA production with over 90% FE at 1.2 A cm⁻², and a remarkable 77.4% carbon efficiency at 0.5 A cm⁻², maintaining stability over 300 h of continuous CO_2R operation at pH = 1. In situ electrochemical ATR-FTIR spectroscopy validates an approximately 2.8× enhancement in *OCHO coverage on Cu_6Sn_5 compared to the control catalyst of Sn, operating under identical electrochemical conditions at pH = 1. Furthermore, using an SSE-based MEA electrolyzer, we stably produce pure FA solution with a concentration of 0.36 M over a 130-hour reaction at a full-cell energy

efficiency surpassing 37%. We expect that the insights gained from our work, particularly in the context of optimizing intermediate adsorption and coverage, will provide valuable guidance for the advancement of selective and energy-efficient CO_2R with long-lasting performance in cation-free, MEA-based electrolyzers.

Methods

Density functional theory (DFT) calculation

DFT calculations were conducted using the Vienna Ab-initio Simulation Package (VASP)[50]. To take the solvation effects into consideration, hybrid solvation effects have been employed in VASPsol along with explicit water molecules at the interface[45–48]. The Constant Electrode Potential (CEP) model has been employed to investigate the constant negative applied potential and cation effects through grand-canonical DFT (GC-DFT) calculations[49]. These calculations were used to compare the energy diagrams of two possible CO_2 reduction reaction (CO_2R) pathways over different surfaces. We have investigated Cu (111), $Cu_{0.86}Sn_{0.14}$ (111), Cu_6Sn_5 (−113), and Sn (100) surfaces for calculations (Supplementary Fig. 4), where these facets are also the most thermodynamic favorable ones for Cu, Sn, and $Cu_{1−x}Sn_x$ alloy systems. More DFT calculation details are included in the Supplementary Information.

Synthesis

We fabricated a series of $Cu_{1−x}Sn_x$ (x = 0.08, 0.14, 0.28, 0.44, 0.71, 0.88), Cu, and Sn electrocatalysts by thermal evaporation (SKY-RH400). Cu and Sn particles were placed separately in two Molybdenum boats inside the deposition chamber and melted slowly under the pressure of 10^{-5} Torr for thermal evaporation. We controlled the thermal evaporation rates of Cu and Sn to adjust the Cu/Sn ratios in the synthesized alloys. Evaporating rates of approximately x Å s⁻¹ (x = 0.08, 0.14, 0.28, 0.44, 0.71, 0.88) for Sn and approximately $(1−x)$ Å s⁻¹ for Cu were used to produce alloyed $Cu_{1−x}Sn_x$ films on the polytetrafluoroethylene (PTFE) substrates. A quartz crystal monitor was used to observe the thicknesses of evaporated $Cu_{1−x}Sn_x$. Evaporation of pure Sn and pure Cu electrocatalysts was conducted using a similar fabrication procedure. The loading of all catalysts is 800 nm thick.

Characterization

Transmission electron microscopy (SEM) images were taken using a Hitachi SU8100 SEM at an accelerating voltage of 5 kV. High-resolution transmission electron microscopy (HRTEM) and transmission electron microscopy-energy dispersive X-ray spectroscopy (TEM-EDX), selected area electron diffraction (SAED), and bright-field and dark-field TEM analyses were performed in a TEM (Tecn F20) with an accelerating voltage of 200 kV. X-ray powder diffraction (XRD) was carried out with a Bruker D8 Advance at a scanning rate of $10°\text{ min}^{-1}$ in the 2θ range from $20°$ to $80°$. X-ray photoelectron spectroscopy (XPS) studies were performed using PHI5000 VersaProbe. The binding energy data were calibrated relative to the C 1 s signal at 284.6 eV.

Electrochemical experiments

Experiments under alkaline and acidic conditions were performed in a flow cell using a three-electrode system. Ag/AgCl electrode was used as the reference electrode, commercial Ni foam (for use under alkaline conditions) and Pt (for use under acidic conditions) were used as the counter electrodes, $Cu_{1-x}Sn_x$ ($x = 0.08, 0.14, 0.28, 0.44, 0.71, 0.88$), Cu, and Sn on PTFE electrodes were used as the working electrodes (area: 0.5 cm^2), and the electrolytes were 1 M KOH (for alkaline CO_2 electrolysis) and $0.05\text{ M }H_2SO_4$ with 3 M KCl (for acidic CO_2 electrolysis). Anion exchange membrane (Fumasep FAB-PK-130, size: $2 \times 2\text{ cm}^2$, thickness: $130\ \mu\text{m}$) and proton exchange membrane (Nafion N117, size: $2 \times 2\text{ cm}^2$, thickness: $183\ \mu\text{m}$) were used as the ion exchange membranes. The proton exchange membrane was immersed in $0.5\text{ M }H_2SO_4$ for about 2 h before use. Experiments using solid-state electrolyte (SSE) were performed in a membrane electrode assembly (MEA) system with a 1 mm-thick SSE layer between the cathode and anode. IrO_x/Ti foam was used as the anode, and Cu_6Sn_5 was used as the cathode (area: 4 cm^2). Anion exchange membrane (Sustainion X37-50 Grade, size: $4 \times 4\text{ cm}^2$, thickness: $50\ \mu\text{m}$) and proton exchange membrane (Nafion N117, size: $4 \times 4\text{ cm}^2$, thickness: $183\ \mu\text{m}$) were used as the ion exchange membranes. The SSE was AmberChrom 50WX4 hydrogen form (J&K Scientific), and the anolyte was $0.5\text{ M }H_2SO_4$. The electrochemical workstation was Autolab PGSTAT302N (Metrohm). The gas flow rate was controlled at 25 mL min^{-1} by an electronic flow meter, and the end flow rate was calibrated by a soap film flow meter during the test.

All of the electrode potentials vs. the Ag/AgCl electrode were converted to the potentials vs. reversible hydrogen electrode (RHE) using the following Eq. (1):

$$E_{RHE} = E_{Ag/AgCl} + 0.197 + 0.059 \times pH + iR \qquad (1)$$

Gas-phase products were measured using gas chromatography (GC Agilent 990, Perkin Elmer Clarus 680). According to the peak area, the Faradaic efficiency of the gas products can be obtained, and the calculation formula is as the following Eq. (2):

$$FE = \frac{F \times z \times v \times n}{I \times t} \times 100\% \qquad (2)$$

where F is the Faraday's constant, which is 96485 C mol^{-1}. z is the number of electrons required to reduce CO_2 to a CO or H_2 molecule, which is 2. v is the gas flow rate, here is 25 mL min^{-1}. n is the concentration of the gas products obtained by GC with 1 mL of sample gas, the unit is mol mL^{-1}. I is the current applied to the sample, the unit is A. t is the reaction time, and the unit is s.

Liquid product $HCOO^-$ was measured using ion chromatography (IC, SH-AC-11, Qingdao shenghan). The FE towards formate or FA at each current density was calculated by adding up both anodic and cathodic FEs. We first obtained a standard curve with a concentration gradient of sodium formate (HCOONa), $HCOO^-$ concentrations were set as 1 ppm, 2 ppm, 5 ppm, 10 ppm, 50 ppm, and 100 ppm (mg L^{-1}).

According to this, the $HCOO^-$ concentration in the electrolyte after the reaction can be obtained. The formula of faradaic efficiency calculation for $HCOO^-$ is as the following Eq. (3):

$$FE = \frac{F \times z \times V \times n}{45 \times I \times t} \times 100\% \qquad (3)$$

where F is the Faraday's constant, which is 96485 C mol^{-1}. n is the concentration of $HCOO^-$ measured by the instrument based on the standard curve, and the unit is mg L^{-1}. z is the number of electrons required for the reduction of CO_2 into $HCOO^-$, here is 2. V is the volume of the catholyte, here is 0.03 L. t is the reaction time, and the unit is s.

All data, including Faradaic efficiencies, were collected based on 1-hour electrolysis. Stability tests were conducted over 300 h. The overpotential is determined by subtracting the operating potential at specific current densities for formic acid generation from the theoretic potential for formic acid production, which is -0.199 V_{RHE}. In situ electrochemical attenuated total reflection Fourier-transform infrared spectroscopy (ATR-FTIR) experiments were conducted on a Thermo Scientific Nicolet 6700 FTIR spectrometer with ZnSe as the prismatic window at room temperature. A three-electrode electrochemical single-cell was used for the tests (Supplementary Fig. 57). The thermally-evaporated Cu_6Sn_5 catalyst on a carbon gas diffusion layer (Freudenberg H15C13) was used as the working electrode, a Pt wire was used as the counter electrode, and a saturated Ag/AgCl electrode was used as the reference electrode. 3 M KCl and $0.05\text{ M }H_2SO_4$ (pH = 1) saturated with CO_2 was used as the electrolyte. Open circuit potential (OCP) was conducted as a comparison, and the data was collected using chronoamperometric tests from -0.24 to -1.64 V_{RHE}. The peak area of $^*OCHO$ in FTIR was calculated by integrating the corresponding curve areas in the same interval ($1250–1500\text{ cm}^{-1}$) obtained at different potentials. More experimental details are discussed in the Supplementary Information.

Data availability

Source data to generate figures and tables are available from the corresponding authors.

References

1. Montoya, J. H. et al. Materials for solar fuels and chemicals. *Nat. Mater.* **16**, 70–81 (2017).
2. Urbain, F. et al. Multijunction Si photocathodes with tunable photovoltages from 2.0 V to 2.8 V for light induced water splitting. *Energy Environ. Sci.* **9**, 145–154 (2016).
3. Mistry, H. et al. Nanostructured electrocatalysts with tunable activity and selectivity. *Nat. Rev. Mater.* **1**, 16009 (2016).
4. Ulas, B. & Kivrak, H. D. Direct formic acid and formate fuel cells (DF(A)FCs). in *Direct Liquid Fuel Cells*. 149–176 (Elsevier, Amsterdam, The Netherlands, 2021).
5. Pérez-Fortes, M. et al. Formic acid synthesis using CO_2 as raw material: Techno-economic and environmental evaluation and market potential. *Int. J. Hydrog. Energy* **41**, 16444–16462 (2016).
6. Ma, W. et al. Promoting electrocatalytic CO_2 reduction to formate via sulfur-boosting water activation on indium surfaces. *Nat. Commun.* **10**, 892 (2019).
7. Pan, B. et al. Close to 90% single-pass conversion efficiency for CO_2 electroreduction in an acid-fed membrane electrode assembly. *ACS Energy Lett.* **7**, 4224–4231 (2022).
8. Huang, J. E. et al. CO_2 electrolysis to multicarbon products in strong acid. *Science* **372**, 1074–1078 (2021).
9. Jiang, M. et al. Rapid and green electric-explosion preparation of spherical indium nanocrystals with abundant metal defects for highly-selective CO_2 electroreduction. *Nano Lett.* **23**, 291–297 (2023).

10. Yang, Z. et al. P-block metal-based (Sn, In, Bi, Pb) electrocatalysts for selective reduction of CO_2 to formate. *APL Mater.* **8**, 060901 (2020).

11. Yan, S. et al. Electron localization and lattice strain induced by surface lithium doping enable ampere-level electrosynthesis of formate from CO_2. *Angew. Chem. Int. Ed.* **60**, 25741–25745 (2021).

12. Li, L. et al. Achieving high single-pass carbon conversion efficiencies in durable CO_2 electroreduction in strong acids via electrode structure engineering. *Angew. Chem. Int. Ed.* **62**, e202300226 (2023).

13. Dinh, C. T. et al. CO_2 electroreduction to ethylene via hydroxide-mediated copper catalysis at an abrupt interface. *Science* **360**, 783–787 (2018).

14. Yang, K. D. et al. Morphology-directed selective production of ethylene or ethane from CO_2 on a Cu mesopore electrode. *Angew. Chem. Int. Ed.* **129**, 814–818 (2017).

15. Shen, H. et al. Acidic CO_2-to-HCOOH electrolysis with industrial-level current on phase engineered tin sulfide. *Nat. Commun.* **14**, 2843 (2023).

16. Zhong, M. et al. Accelerated discovery of CO_2 electrocatalysts using active machine learning. *Nature* **581**, 178–183 (2020).

17. Zhang, J. et al. Accelerating electrochemical CO_2 reduction to multi-carbon products via asymmetric intermediate binding at confined nanointerfaces. *Nat. Commun.* **14**, 1298 (2023).

18. Fan, M. et al. Cationic-group-functionalized electrocatalysts enable stable acidic CO_2 electrolysis. *Nat. Catal.* **6**, 763–772 (2023).

19. Xia, C. et al. Continuous production of pure liquid fuel solutions via electrocatalytic CO_2 reduction using solid-electrolyte devices. *Nat. Energy* **4**, 776–785 (2019).

20. Qiao, Y. et al. Engineering the local microenvironment over Bi nanosheets for highly selective electrocatalytic conversion of CO_2 to HCOOH in strong acid. *ACS Catal.* **12**, 2357–2364 (2022).

21. Zheng, T. et al. Copper-catalysed exclusive CO_2 to pure formic acid conversion via single-atom alloying. *Nat. Nanotechnol.* **16**, 1386–1393 (2021).

22. Feaster, J. T. et al. Understanding selectivity for the electrochemical reduction of carbon dioxide to formic acid and carbon monoxide on metal electrodes. *ACS Catal.* **7**, 4822–4827 (2017).

23. Ding, P. et al. Metal-based electrocatalytic conversion of CO_2 to formic acid/formate. *J. Mater. Chem. A* **8**, 21947–21960 (2020).

24. Ren, M. et al. CO_2 to formic acid using Cu-Sn on laser-induced graphene. *ACS Appl. Mater. Interfaces* **12**, 41223–41229 (2020).

25. Morimoto, M. et al. Electrodeposited Cu-Sn alloy for electrochemical CO_2 reduction to CO/HCOO⁻. *Electrocatalysis* **9**, 323–332 (2018).

26. Li, D. et al. Facile synthesis of porous Cu-Sn alloy electrode with prior selectivity of formate in a wide potential range for CO_2 electrochemical reduction. *Appl. Catal. B: Environ.* **292**, 120119 (2021).

27. Chen, Z. et al. 3D hierarchical porous structured carbon nanotube aerogel-supported Sn spheroidal particles: an efficient and selective catalyst for electrochemical reduction of CO_2 to formate. *J. Mater. Chem. A* **5**, 24651–24656 (2017).

28. Liang, C. et al. High efficiency electrochemical reduction of CO_2 beyond the two-electron transfer pathway on grain boundary rich ultra-small SnO_2 nanoparticles. *J. Mater. Chem. A* **6**, 10313–10319 (2018).

29. Fan, L. et al. Electrochemical CO_2 reduction to high-concentration pure formic acid solutions in an all-solid-state reactor. *Nat. Commun.* **11**, 3633 (2020).

30. Grigioni, I. et al. CO_2 Electroreduction to formate at a partial current density of 930 mA cm⁻² with InP colloidal quantum dot derived catalysts. *ACS Energy Lett.* **6**, 79–84 (2021).

31. Lei, F. et al. Metallic tin quantum sheets confined in graphene toward high-efficiency carbon dioxide electroreduction. *Nat. Commun.* **7**, 12697 (2016).

32. García De Arquer, F. P. et al. 2D metal oxyhalide-derived catalysts for efficient CO_2 electroreduction. *Adv. Mater.* **30**, 1802858 (2018).

33. Chen, Y. et al. A robust, scalable platform for the electrochemical conversion of CO_2 to formate: identifying pathways to higher energy efficiencies. *ACS Energy Lett.* **5**, 1825–1833 (2020).

34. Kopljar, D. et al. Transferring electrochemical CO_2 reduction from semi-batch into continuous operation mode using gas diffusion electrodes. *Chem. Eng. Technol.* **39**, 2042–2050 (2016).

35. Löwe, A. et al. Optimizing reaction conditions and gas diffusion electrodes applied in the CO_2 reduction reaction to formate to reach current densities up to 1.8 A cm⁻². *ACS Sustain. Chem. Eng.* **9**, 4213–4223 (2021).

36. Del Castillo, A. et al. Sn nanoparticles on gas diffusion electrodes: Synthesis, characterization and use for continuous CO_2 electroreduction to formate. *J. CO2 Util.* **18**, 222–228 (2017).

37. Sen, S. et al. Electroreduction of carbon dioxide to formate at high current densities using tin and tin oxide gas diffusion electrodes. *J. Appl. Electrochem.* **49**, 917–928 (2019).

38. Wu, D. et al. Boosting formate production at high current density from CO_2 electroreduction on defect-rich hierarchical mesoporous Bi/Bi_2O_3 junction nanosheets. *Appl. Catal. B: Environ.* **271**, 118957 (2020).

39. Rabiee, H. et al. Tuning the product selectivity of the Cu hollow fiber gas diffusion electrode for efficient CO_2 reduction to formate by controlled surface Sn electrodeposition. *ACS Appl. Mater. Interfaces* **12**, 21670–21681 (2020).

40. Xing, Y. et al. Bi@Sn core–shell structure with compressive strain boosts the electroreduction of CO_2 into formic acid. *Adv. Sci.* **7**, 1902989 (2020).

41. Creissen, C. E. et al. Molecular inhibition for selective CO_2 conversion. *Angew. Chem. Int. Ed.* **61**, e202206279 (2022).

42. Wang, W. et al. In situ phase separation into coupled interfaces for promoting CO_2 electroreduction to formate over a wide potential window. *Angew. Chem. Int. Ed.* **60**, 22940–22947 (2021).

43. Yang, Q. et al. Novel Bi-doped amorphous SnO_x nanoshells for efficient electrochemical CO_2 reduction into formate at low overpotentials. *Adv. Mater.* **32**, 2002822 (2020).

44. Ma, X. et al. Facet dopant regulation of Cu_2O boosts electrocatalytic CO_2 reduction to formate. *Adv. Funct. Mater.* **33**, 2213145 (2023).

45. Mathew, K. et al. Implicit self-consistent electrolyte model in plane-wave density-functional theory. *J. Chem. Phys.* **151**, 234101 (2019).

46. Petrosyan, S. A. et al. Joint density-functional theory: Ab initio study of Cr_2O_3 surface chemistry in solution. *J. Phys. Chem. B* **109**, 15436–15444 (2005).

47. Mathew, K. et al. Implicit solvation model for density-functional study of nanocrystal surfaces and reaction pathways. *Chem. Phys.* **140**, 084106 (2014).

48. Goodpaster, J. D. et al. Identification of possible pathways for C–C bond formation during electrochemical reduction of CO_2: new theoretical insights from an improved electrochemical model. *J. Phys. Chem. Lett.* **7**, 1471–1477 (2016).

49. Hormann, N. G. et al. Grand canonical simulations of electrochemical interfaces in implicit solvation models. *J. Chem. Phys.* **150**, 041730 (2019).

50. Kresse, G. & Hafner, J. Ab initio molecular dynamics for liquid metals. *Phys. Rev. B: Condens. Matter* **47**, 558–561 (1993).

Acknowledgements

Author contributions

Competing interests

The authors declare no competing interests.

Additional information

Supplementary information The online version contains supplementary material available at
https://doi.org/10.1038/s41467-024-45988-4.

Correspondence and requests for materials should be addressed to Fanglin Che or Miao Zhong.

Peer review information *Nature Communications* thanks the anonymous reviewers for their contribution to the peer review of this work. A peer review file is available.

Reprints and permissions information is available at
http://www.nature.com/reprints

Publisher's note Springer Nature remains neutral with regard to jurisdictional claims in published maps and institutional affiliations.